Dynamics of Atmospheres and Oceans 90 (2020) 101145

Contents lists available at ScienceDirect

Dynamics of Atmospheres and Oceans

journal homepage: www.elsevier.com/locate/dynatmoce

Subseasonal coupling between subsurface subtropical front and overlying atmosphere in North pacific in winter

FeiFei Chen[a], HaiBo Hu[a,b,*], Haokun Bai[a]

[a] CMA-NJU Joint Laboratory for Climate Prediction Studies, Instituted for Climate and Global Change Research, School of Atmospheric Science, Nanjing University, Nanjing 210093, China
[b] KLME & CIC-FEMD, Nanjing University of Information Science and Technology, Nanjing, China

ARTICLE INFO

Keywords:
Subsurface subtropical front
Subseasonal air-sea coupled process
Positive air-sea feedback
Subtropical countercurrent
Atmospheric baroclinic eddy growth rate

ABSTRACT

At least two main oceanic fronts (the subarctic and subtropical fronts) exist in the North Pacific. Especially in the subtropical frontal zone (STFZ), the sea subsurface temperature gradient is significantly larger than that of the surface layer in winter. Subseasonal interaction between the subsurface subtropical front and overlaying atmosphere is revealed by using empirical orthogonal function (EOF) analysis of oceanic temperature gradient. The first EOF mode mainly corresponds to the atmosphere-to-ocean influences. With the enhanced westerly wind, a cold sea surface temperature anomaly (SSTA) appears and then passes down to affect the subsurface ocean. However, the second EOF mode indicates the ocean-to-atmosphere forcing. For the second mode, cold oceanic temperature anomaly generates in the subsurface layer and passes up, which makes the SST gradient increasing. Due to the increasing atmospheric baroclinicity, the enhanced westerly wind leads to more heat fluxes from the ocean to the atmosphere, which results in a colder SSTA and a larger SST gradient in the STFZ. Therefore, a positive ocean-atmosphere feedback begins to maintain in the mid-latitude in winter.

1. Introduction

Oceanic fronts associated with SST anomalies are considered to be a key region for the mid-latitude ocean affecting the overlying atmosphere. Lots of studies have identified that oceanic fronts have a remarkable impact on the regional climate and weather system (Wallace et al., 1990; Vecchi et al., 2004; Tokinaga et al., 2006; Small et al., 2008; Liu et al., 2016).

For the basin scale, a significant negative correlation exists between SST and surface wind (Namias and Cayan, 1981). Negative (positive) SST anomalies often occur where the surface wind speed increases (weakens) (Wallace et al., 1990). The negative correlation indicates the influence of the atmosphere on the ocean, which can be explained by heat flux changes (Alexander et al., 2002; Xie, 2004). Owing to the development of high-resolution observations and numerical simulations, a deeper understanding of the small-scale air-sea interaction went up (Hashizume et al., 2002; Minobe et al., 2008). A completely different SST-wind relationship was found over the small-scale SST frontal zone, which represents the ocean-to-atmosphere forcing (Tokinaga et al., 2006; Shimada and Kawamura, 2008; Liu et al., 2013; Xu et al., 2011; Xu and Xu, 2015). A positive correlation between SST and surface wind was observed in the Antarctic Circumpolar Current region (O'Neill et al., 2003; Annis and White, 2003), the Somali Current region (Vecchi et al., 2004), the Gulf Stream region (Parfitt et al., 2016) and the Kuroshio Extension region (Yao et al., 2016; Hirata et al., 2016).

* Corresponding author.
E-mail address: huhaibo@nju.edu.cn (H. Hu).

https://doi.org/10.1016/j.dynatmoce.2020.101145
Received 18 December 2019; Received in revised form 4 April 2020; Accepted 18 April 2020
Available online 21 April 2020

SST anomaly in the oceanic front not only influences the surface wind speed, but also plays an important role in the formation and development of transient eddy in the storm tracks (Small et al., 2014; Parfitt et al., 2016). The sensible heat flux difference on both sides of the front can effectively maintain the near-surface baroclinicity and anchor the storm tracks in the midlatitude atmosphere (Nakamura et al., 2008). The variability of SST fronts can also influence the atmospheric circulation. Yao et al. (2016) changed the intensity of subarctic front zone (SAFZ) in sensitivity experiments and confirmed that the storm tracks can be intensified as a response to the enhanced SAFZ. Wang et al. (2016, 2018) and Zhang et al. (2017) investigated the relationship between the variability of subtropical front zone (STFZ) intensity and the East Asian jet stream (EAJS). The results suggested that the lower-level temperature gradient and atmospheric baroclinicity enhanced with STFZ intensifying, resulting in more active transient eddy forcing and thus a reinforcement of the EAJS. Chen et al. (2019) found that atmospheric baroclinicity gets stronger rapidly through upward sensible heat flux (SHF) after the STFZ enhancement. The strengthened storm tracks arouse more and stronger Rossby Wave Breaking (RWB) events in the upper troposphere, resulting in more transient perturbation kinetic energy transported to the mean flow, accelerating the westerly finally.

At present, more attention is paid to the impacts of SAFZ, research on STFZ mostly focus on the field of oceanography. Two kinds of front exist in STFZ in North Pacific, the subsurface front located at the depth of about 100 − 200 meters and the surface front located at the sea surface (Aoki et al., 2002). The subsurface front is stable all year round, while the surface front is strongest in winter and spring (Kobashi et al., 2006, 2012; Qiu et al., 2015). Kobashi et al. (2006, 2012) found three subtropical countercurrents (STCC) in North Pacific and they each accompany a temperature and density front at subsurface depths of about 100 − 200 m. Observational studies often related subtropical fronts (STFs) to the distribution of mode water. Suga and Hanawa (1990) pointed out that the position of STF corresponds to the southern edge of the Subtropical Mode Water (STMW). Aoki et al. (2002) suggested that the collocation of STF and southern edge of low potential vorticity (PV) water supports the mechanism of Kubokawa and Inui (1999). The vertical accumulation of low PV water causes the upper thermocline to rise, leading to an eastward countercurrent on the southern edge of the low-PV pool. Then, the isopycnic surface in the upper thermocline shallows northward because of the STMW, the STF forms. This mechanism was also confirmed in the numerical experiments (Xu et al., 2012).

Previous studies mostly focused on the relationship between sea surface front and overlying atmosphere, but the role of the subsurface front cannot be ignored. How will the subsurface subtropical front affect the upper ocean and the overlying atmosphere? Will the atmosphere influence the subsurface front intensity in response? To settle above questions, Climate Forecast System Reanalysis (CFSR) dataset was used to analyze the relationship between subsurface subtropical front and overlying atmosphere. The rest of the paper is organized as follows. Data is described in Section 2. Spatial distribution of oceanic temperature gradient is shown in Section 3. Two different air-sea coupled progresses are estimated in Section 4. The summary and discussion are presented in Section 5.

2. Data and method

CFSR dataset is a high-resolution reanalysis data provided by National Centers for Environmental Prediction (NCEP). It is designed and executed as a global, high-resolution, coupled atmosphere-ocean-land surface-sea ice system to provide the best estimate of the states of these coupled domains (Saha et al., 2010). Here, we use daily data calculated from the 6 -hly products during the wintertime (December-February) of 1979–2009 with a horizontal grid spacing of 0.5°. The oceanic product has 40 vertical levels from 4478 m to 5 m below sea level and the atmospheric product has 37 vertical pressure levels from 1000 hPa to 1 hPa.

Considering Guan et al. (2019) and Bai et al. (2019) have confirmed the reasonability of using the continuous wintertime or summertime physical quantity, we performed EOF analysis on continuous wintertime oceanic temperature gradient in this study. We first subtracted the corresponding winter mean in each year to remove the inter-annual variation, then subtracted the 31-year mean to remove the seasonal variation, and finally took a 5-day running mean. North test is used to test if an EOF mode is separated from its neighboring modes. Assume $X=\begin{pmatrix} x_{1,1} & \cdots & x_{1,N} \\ \vdots & \ddots & \vdots \\ x_{M,1} & \cdots & X_{M,N} \end{pmatrix}$ is the matrix of the physical quantity, where M means the number of grid points and N means the length of its time series. λ_1 and λ_2 are eigenvalues of the first and second modes, respectively. According to North et al. (1982), when $\lambda_1(2/N)^{1/2} < \lambda_1 - \lambda_2$, the first mode is separated. Similarly, we can prove the separation of other modes.

Lead-Lag regression is used in this study. Day 0 means simultaneous regression. A negative lag day (a positive lag day) is performed by shifting backward (forward) the number of the leading (lag) days. For regression results, we perform the significant test on the regression coefficient. Standardized time series of the mode is used as x_i, time series of physical quantity is used as y_i. When the time series contains n days, the statistics t follows t-distribution with (n_e-2) degrees of freedom.

$$t = \frac{\frac{b}{\sqrt{c}}}{\sqrt{\frac{Q}{n_e - 2}}}$$

Where, $b = \frac{\sum_{i=1}^{n}(x_i - \bar{x})(y_i - \bar{y})}{\sum_{i=1}^{n}(x_i - \bar{x})^2}$, $c = [\sum_{i=1}^{n}(x_i - \bar{x})^2]^{-1}$, $Q = \sum_{i=1}^{n}(y_i - \hat{y}_i)^2$.The equivalent degree of freedom is estimated using $n_e = n * \frac{1 - r_1}{1 + r_1}$, where r_1 is the lag-one autocorrelation. It should be noted that if r_1 is not significant, $n_e = n$. For given significant level ($\alpha = 0.05$) and degrees of freedom (n_e-2), we can find the corresponding critical value t_α. If $t > t_\alpha$, we reject the null hypothesis and think the differences are significant.

For composite results, we test the credibility of the differences between typical events of each mode and general events. When

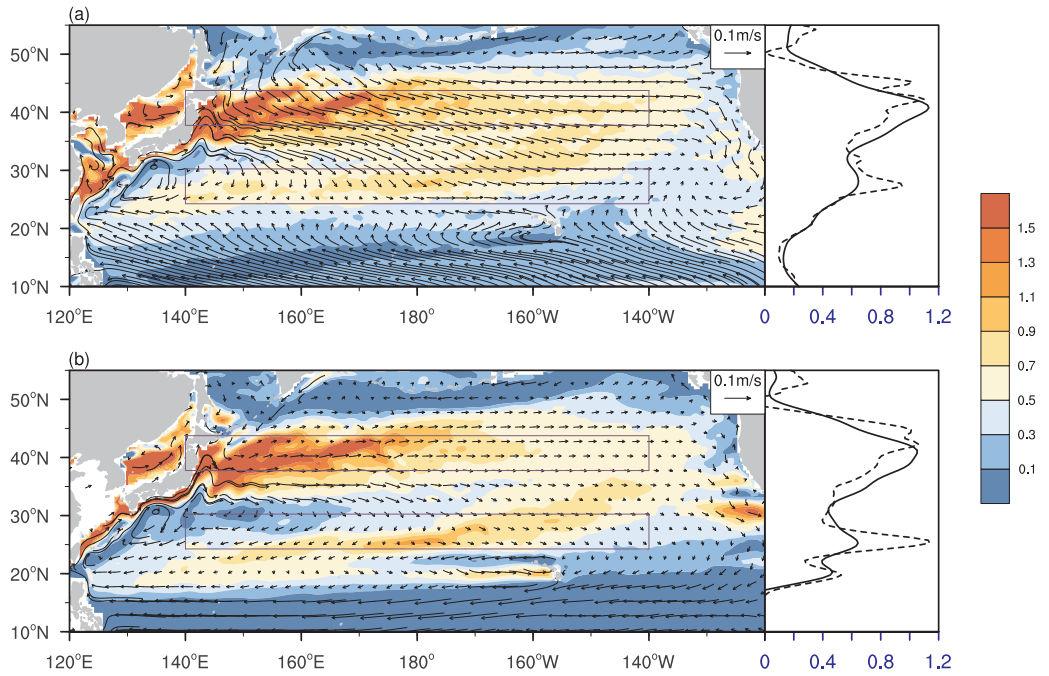

Fig. 1. Distribution of climatological wintertime meridional temperature gradient (shadings, unit: ℃/100 km) and current (arrows, unit: m/s) at (a) sea surface, (b) 100-meter depth. The solid line on the right is the latitudinal average (140 °E-140 °W) temperature gradient (unit, ℃/100 km). The dotted line is the temperature gradient (unit, ℃/100 km) at 180°. The purple frame is the location of the oceanic front.

there are n typical events and m general events, the statistics t follows t-distribution with ($n_e + m_e$-2) degrees of freedom. s^2 means the unbiased estimator of the variance of the difference. x_i^a and x_i^c mean the daily data of typical events and general events relatively.

$$t = \frac{\bar{x^c} - \bar{x^a}}{s\sqrt{\frac{1}{m_e} + \frac{1}{n_e}}}$$

$$s^2 = \frac{\sum_{i=1}^{n}(x_i^c - \bar{x^c})^2 + \sum_{i=1}^{m}(x_i^a - \bar{x^a})^2}{n_e + m_e - 2}$$

The calculation method of equivalent degrees of freedom n_e, m_e is consistent with the above. For given significant level ($\alpha = 0.05$) and degrees of freedom ($n_e + m_e$-2), we can find the corresponding critical value t_α. If $t > t_\alpha$, we reject the null hypothesis and think the differences are significant.

3. Spatial distribution of oceanic temperature gradient

Two SST fronts distributed in a meridionally-narrow and zonally-elongated manner over the North Pacific basin, while SAFZ locates at about 38 °N-44 °N and STFZ locates at about 24 °N-30 °N (Fig. 1a). The SAFZ is stronger than STFZ. Large values of oceanic temperature gradient also exist along the two frontal zones at the depth of 100 m (Fig. 1b). Moreover, the oceanic temperature gradient at the depth of 100 m is larger than the SST gradient in the STFZ, however, quite similar in the SAFZ. Is the SST gradient the largest in SAFZ? Does the largest oceanic temperature gradient occur at the depth of 100 m in STFZ?

In order to find out where the largest oceanic temperature gradient appears, we analyze the vertical distribution of oceanic temperature gradient in the SAFZ (38 °N-44 °N) and STFZ (24 °N-30 °N). The SST gradient is relatively large in the SAFZ (Fig. 2a). The largest oceanic temperature gradient appears at the depth of 80–160 meters in the STFZ, where the oceanic temperature gradient and the zonal current are well-configured (Fig. 2b). This indicates that the formation of the subsurface subtropical front may be related to the subtropical countercurrent. Then, we wonder whether the subsurface subtropical front can influence the SST and SST gradients. The typical case from Dec 24th, 1987 to Jan 1 st, 1988 shows a process that the cold temperature anomaly passes down from the surface layer to the subsurface layer. However, the other case from Dec 4th, 1988 to Dec 12th, 1988 shows a process that the cold temperature anomaly passes up from the subsurface layer to the surface layer, which suggests the subsurface subtropical front influence on sea surface (Fig. 3). These two different cases indicate that different physical processes exist between the surface and subsurface layer in the STFZ.

To further explore the specific variability of the oceanic temperature gradient, we performed EOF analysis on continuous wintertime oceanic temperature gradient in the STFZ (24 °N-30 °N). The first two eigenvalues are proved to be separated by North test. The spatial and temporal distributions of the first and second modes are shown in Fig. 4. The third mode is not discussed because of

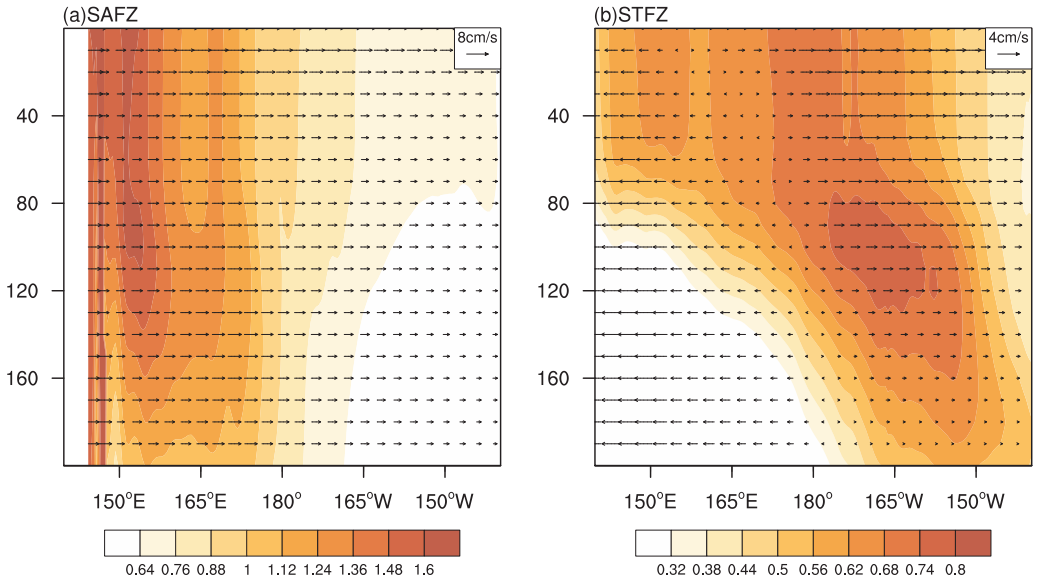

Fig. 2. Vertical distribution of climatological wintertime temperature gradient (shadings, unit: ℃/100 km) and zonal current (arrows, unit: m/s) in (a) SAFZ (38 °N-44 °N), (b) STFZ (24 °N-30 °N).

the small variance. For the first mode, the positive variation appears at the depth of 0–100 meters; while the positive variation appears at the depth of 80–160 meters for the second mode. Besides, the spectrum analysis on time series of Fig. 4c showed that the periods of the first two modes are about 15–30 days. On this subseasonal scale, what physical processes do the two main modes correspond to? We will settle this question in next section.

4. Coupling relationship between subsurface subtropical front and overlaying atmosphere

Known from Fig. 4, the spatial distributions of oceanic temperature gradient for the two main modes are quite different. We suspected that the completely different spatial distributions may correspond to two different air-sea coupled processes. Therefore, we calculated the correlation coefficient between time series of the two modes and found that the correlation coefficient is only $7.67*10^{-10}$, which confirms the hypothesis that the two modes correspond to different air-sea coupled progresses.

4.1. Impact of the atmosphere on the subsurface ocean

In order to analyze the air-sea coupled process that the first mode corresponds to, we used time series of PC1 to perform a lead-lag regression on physical quantities such as oceanic temperature, wind speed and air-sea heat fluxes from day -8 to day 8. Then we subtracted the average of these days to highlight the changes in regression values.

Fig. 5 shows the PC1 lead regression of physical quantities such as oceanic temperature. At day -8, warm oceanic temperature anomaly exists at the surface layer, and the air-sea temperature difference shows a negative anomaly, which corresponds to the heat fluxes transporting from the ocean to the atmosphere. Meanwhile, the westerly wind enhances, leading to the decrease of SST. At day -4, a cold SSTA appears and the westerly wind begins to weaken. However, due to the heat fluxes transporting from the ocean to the atmosphere, SST continues to decrease and reaches a minimum value at day 0. At this time, air-sea temperature difference is quite small, and there is no obvious heat flux transport in the STFZ. PC1 lag regression of oceanic temperature and its gradient in STFZ are shown in Fig. 6. Cold SSTA and positive SST gradient anomaly generate at day 0. From day 0 to day 8, the cold SSTA passes down, leading to the decrease of sea subsurface temperature. This can be verified by the ocean temperature propensity equation:

$$\frac{\partial T_m}{\partial t} = \frac{Q_{net}}{\rho_0 c_p h} - \vec{u}_m \bullet \nabla T_m - \frac{w_e (T_m - T_d)}{h} + E_k$$

where T_m is sea surface temperature and T_d is sea subsurface temperature. Q_{net} is sea surface heat flux, which is the sum of radiative and diffusive heat flux. ρ_0 and c_p are density and specific heat capacity at sea surface respectively. The vertical velocity at the depth of 80 m is used as w_e. We used the oceanic temperature at the depth of 0–80 meters as T_m and the oceanic temperature at the depth of 80–160 meters as T_d. The vertical temperature transport term - $\frac{w_e (T_m - T_d)}{h}$ plays an important role in the interaction between the surface and the subsurface fronts (Fig. 7a). The vertical temperature transport makes the temperature increase at the surface layer at day 0, which means the cold temperature anomaly at the surface layer passes down, making the sea subsurface temperature to decrease (Fig. 7b).

In general, the first mode of EOF analysis is a process in which the atmosphere affects the ocean. By affecting the air-sea heat flux,

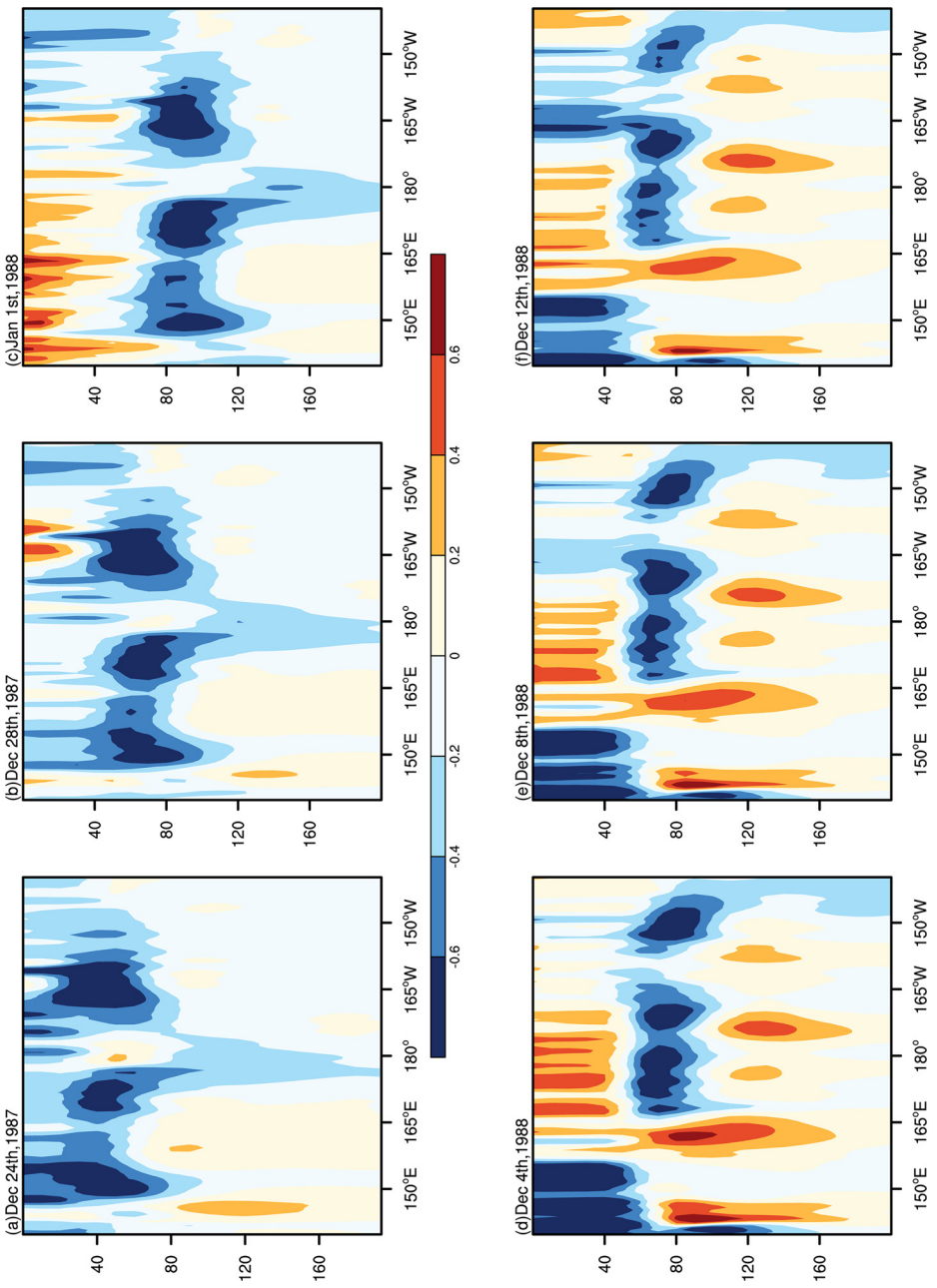

Fig. 3. Spatial distribution of oceanic temperature (shadings, unit: °C) in STFZ (24 °N-30 °N) (a)-(c) from Dec 24th,1987 to Jan 1 st,1988, (d)-(f) from Dec 4th,1988 to Dec 12th,1988.

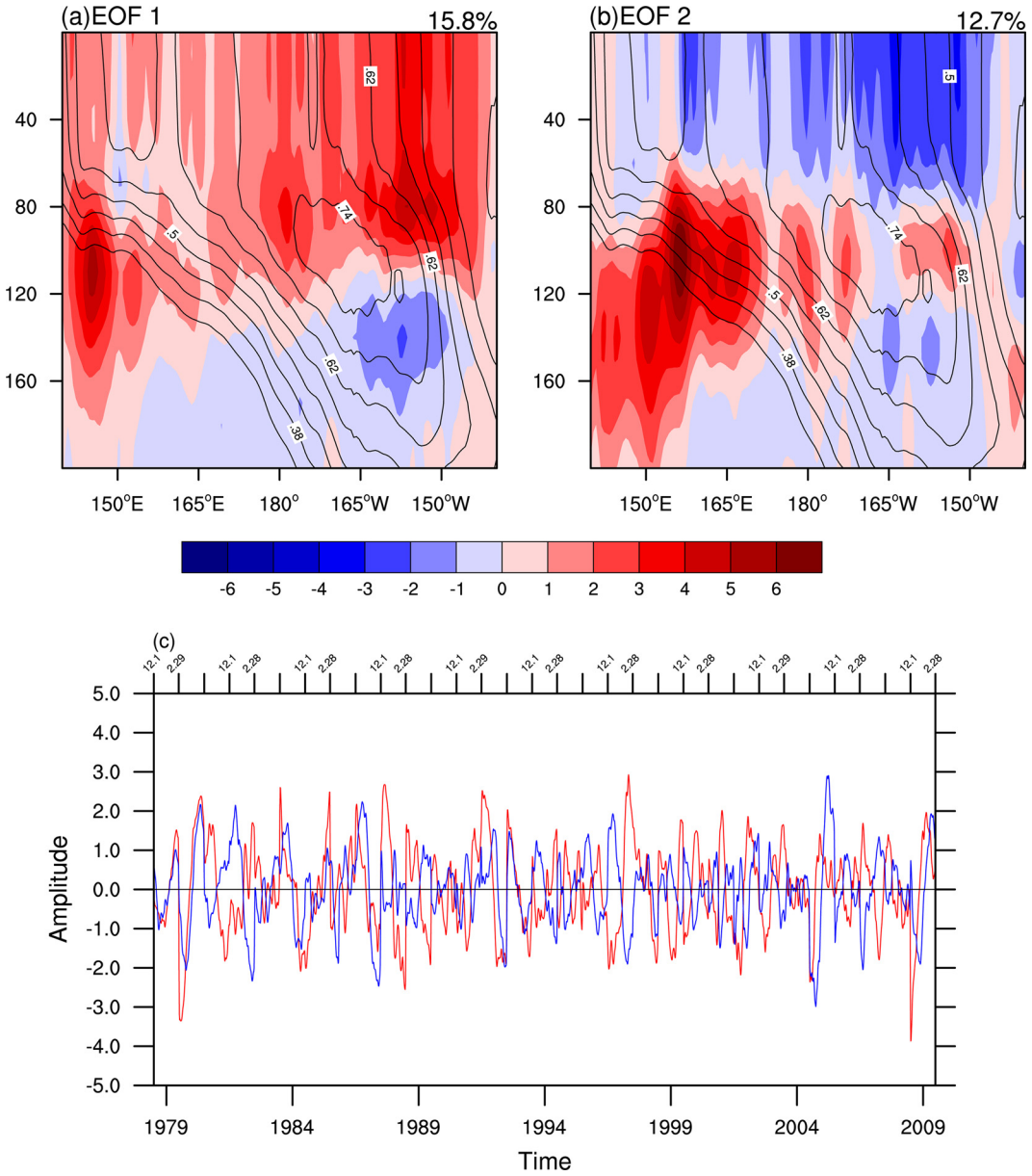

Fig. 4. Spatial distribution of oceanic temperature gradient (shadings, unit: $*10^{-2}$°C/100 km) in STFZ (24 °N-30 °N) for (a) the first mode, (b) the second mode and (c) temporal distribution for the first mode (red line) and second mode (blue line) of EOF analysis on continuous wintertime oceanic temperature gradient. Contours in (a) and (b) are the climatological wintertime temperature gradient in STFZ (unit: °C/100 km).

the westerly wind increasing at day -8 causes a cold SSTA at day 0, and it passes down after day 0, affecting the temperature of the subsurface ocean.

4.2. Impact of the subsurface ocean on the atmosphere

Similar to the first mode, we used time series of PC2 to perform a lead-lag regression on physical quantities such as oceanic temperature, wind speed and air-sea heat flux from day -8 to day 8. Then we subtracted the average of these days.

PC2 lead regression of oceanic temperature and current at the depth of 80–160 meters is shown in Fig. 8. At day -8, the eastward and southward flow increase in the STFZ, thus cold water gradually transports to the frontal zone. The eastward and southward flow spread and cold water continues to transport from day -8 to day 0. It suggests that the cold oceanic temperature anomaly always exists at the subsurface layer. Fig. 9 shows PC2 lead-lag regression of oceanic temperature. The cold oceanic temperature anomaly gradually passes up, and cold oceanic temperature anomaly appears at the surface layer at day 4. Similar to the first mode, the vertical temperature transport term plays an important role in the interaction between the surface and the subsurface fronts. The

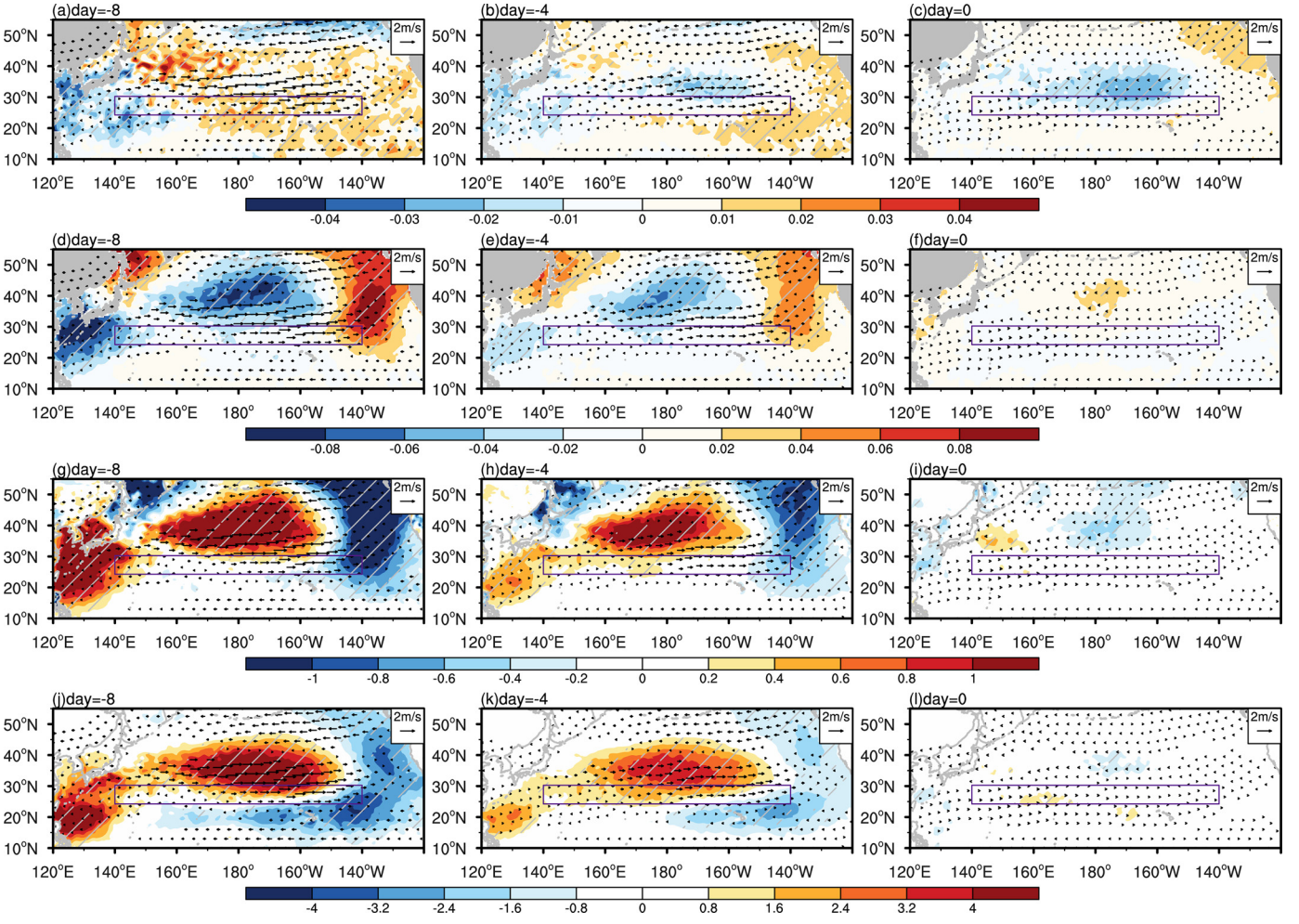

Fig. 5. PC1 lead regression of (a)-(c) sea surface temperature anomaly (shadings, unit: ℃), (d)-(f) air-oceanic temperature difference anomaly (shadings, unit: ℃), (g)-(i) sensible heat flux anomaly (shadings, unit: W/m^2), (j)-(l) latent heat flux anomaly (shadings, unit: W/m^2) and zonal wind anomaly at 200-300 hPa (arrows, unit: m/s). The purple frame is the location of the oceanic front. All arrows drawn passed 0.05 significant level. The areas marked by grey slashes passed the 0.05 significant level.

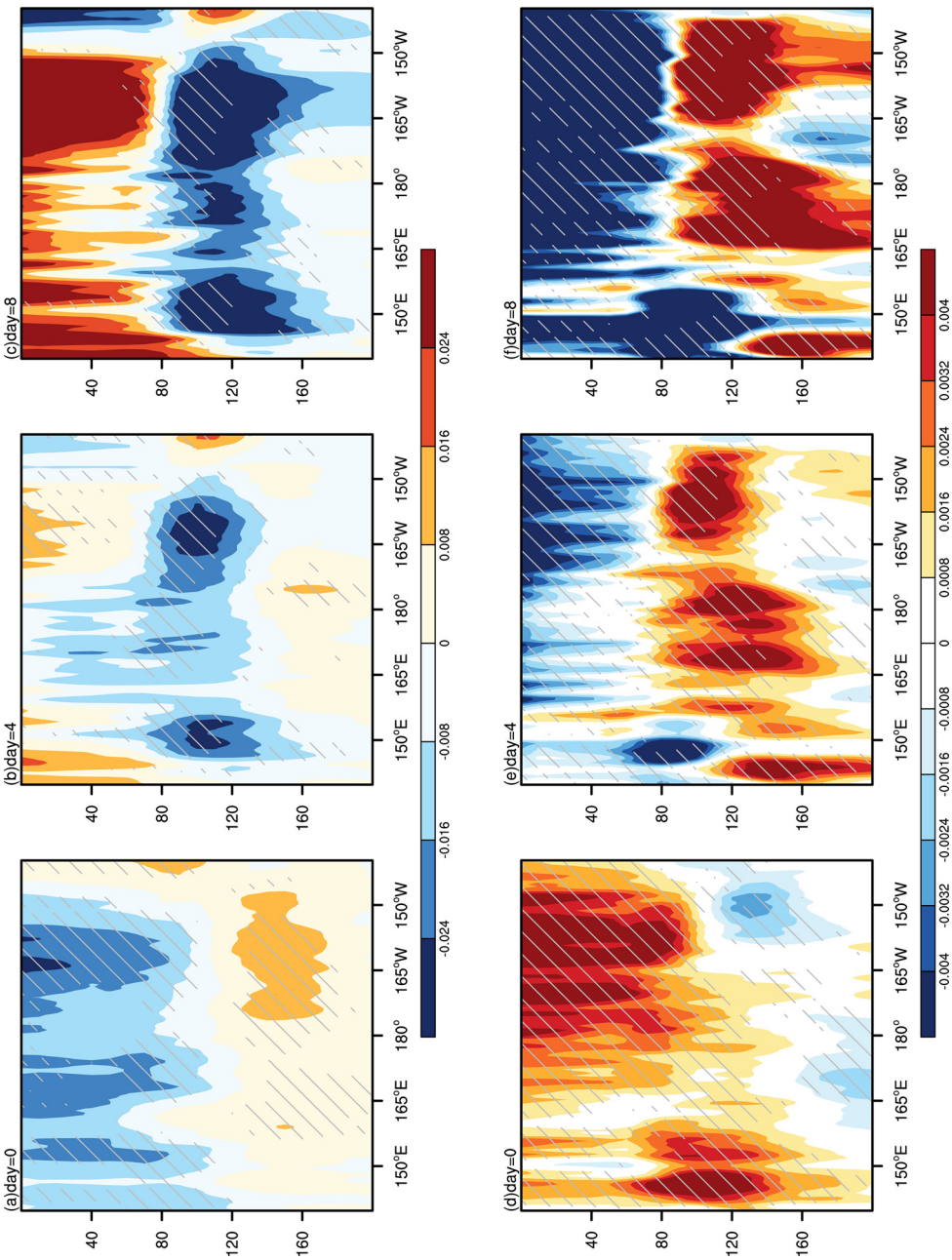

Fig. 6. PC1 lag regression of (a)-(c) oceanic temperature anomaly (shadings, unit: °C) and (d)-(e) oceanic temperature gradient anomaly (shadings, unit: °C/100 km). The areas marked by grey slashes passed the 0.05 significant level.

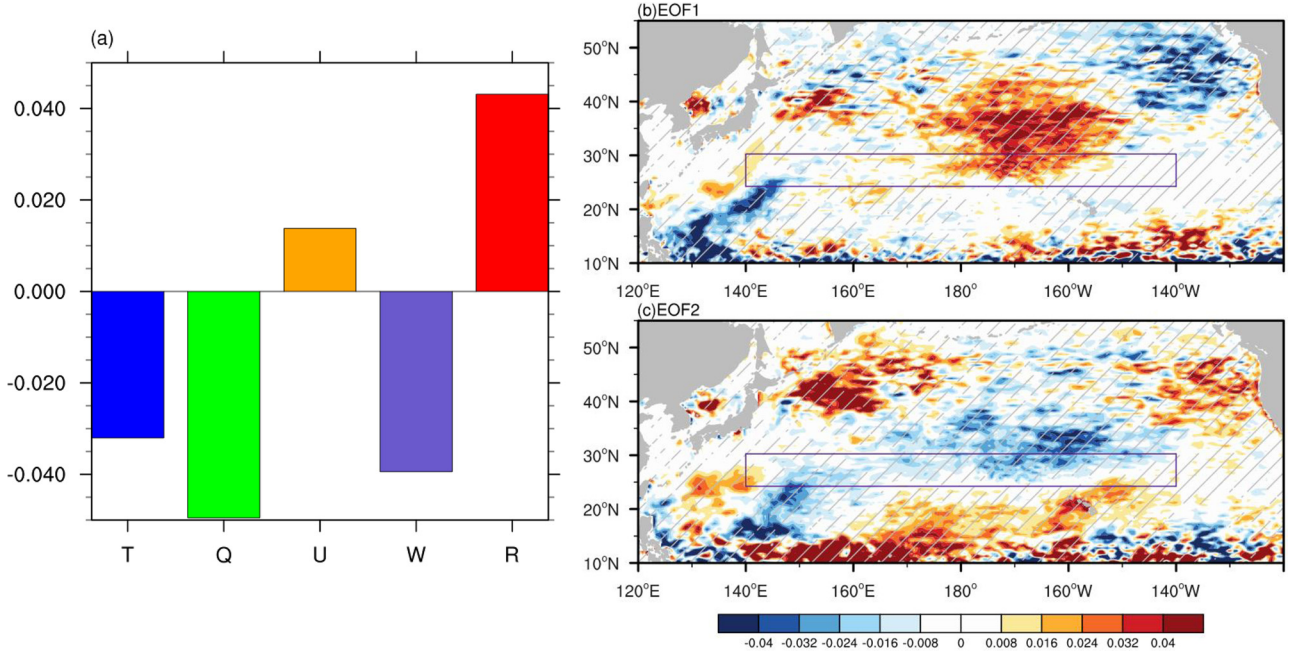

Fig. 7. (a) Terms of ocean temperature propensity equation in STFZ (24°-30 °N, 140 °E-140 °W) (unit:℃/day). T= $\frac{\partial T_m}{\partial t}$, Q= $\frac{Q_{net}}{\rho_0 c_p h}$, U= $-\vec{u}_m \bullet \nabla T_m$, W= $-\frac{w_e(T_m - T_d)}{h}$, E = E_k. (b) Regression of the vertical temperature transport term $-\frac{w_e(T_m - T_d)}{h}$ at the depth of 0-80 m under the first EOF mode (shadings, unit: $*10^{-1}$℃/day). (c) The same as (b) but for the second EOF mode. The purple frame is the location of the oceanic front. The areas marked by grey slashes passed the 0.05 significant level.

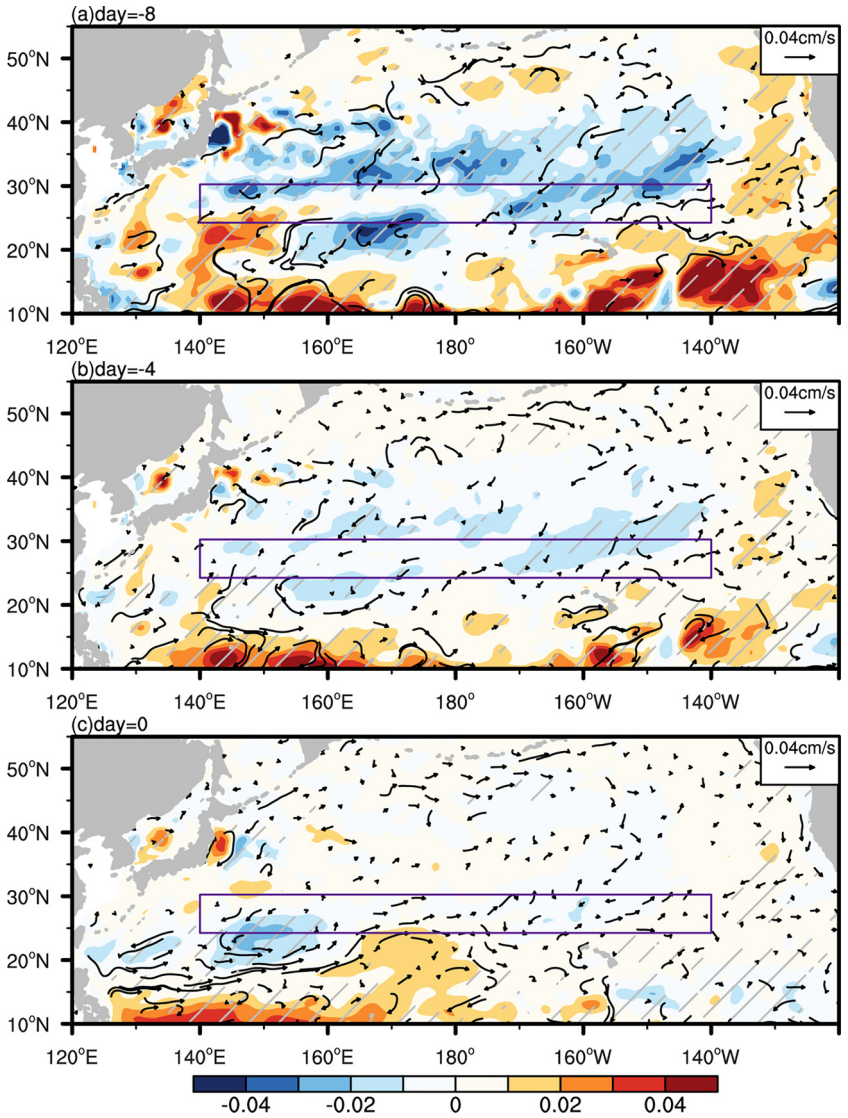

Fig. 8. PC2 lead regression of oceanic temperature anomaly at 80-160 m (shadings, unit: ℃) and current anomaly (arrows, unit: cm/s). The purple frame is the location of the oceanic front. All arrows drawn passed 0.05 significant level. The areas marked by grey slashes passed the 0.05 significant level.

vertical temperature transport makes the temperature decrease at the surface layer, which means the cold temperature anomaly at the subsurface layer passes up (Fig. 7c). To verify the process, we calculated the average oceanic temperature gradient anomaly in the STFZ at different depths (Fig. 10). The oceanic temperature gradient shows a maximum value at day 0 at the depth of 80–160 meters, while a minimum value at the depth of 0–80 meters. After day 0, the sea subsurface temperature gradient decreases, and the SSTA increases, which confirms the vertical temperature transport.

In order to investigate the process of oceanic temperature influencing the atmosphere, we calculated the baroclinic eddy growth rate of the atmosphere, which reflects the atmospheric baroclinicity. Formula of the baroclinic eddy growth rate is as follow:

$$\sigma_{BI} = 0.31\frac{g}{\theta N}\left|\frac{\partial\theta}{\partial y}\right|$$

where $N^2 = -g\alpha\frac{\partial\theta}{\partial p}$, $\alpha = \frac{T}{\theta T_{p=1000}}$. We used the calculated baroclinic eddy growth rate and time series of the second mode to perform a lead-lag regression and subtracted the average of days -8 to 8 (Fig. 11). The baroclinic eddy growth rate shows a positive anomaly near the surface at day 0 in STFZ. Then the anomaly extends from lower troposphere to upper troposphere gradually. This is due to the large oceanic temperature gradient at the subsurface layer passing up, which increases the SST gradient and enhances the atmospheric temperature gradient. Then it spread to the middle and upper troposphere, which makes the baroclinicity eddy growth rate anomaly extend from lower troposphere to upper troposphere. The enhanced atmospheric baroclinicity can finally accelerate the

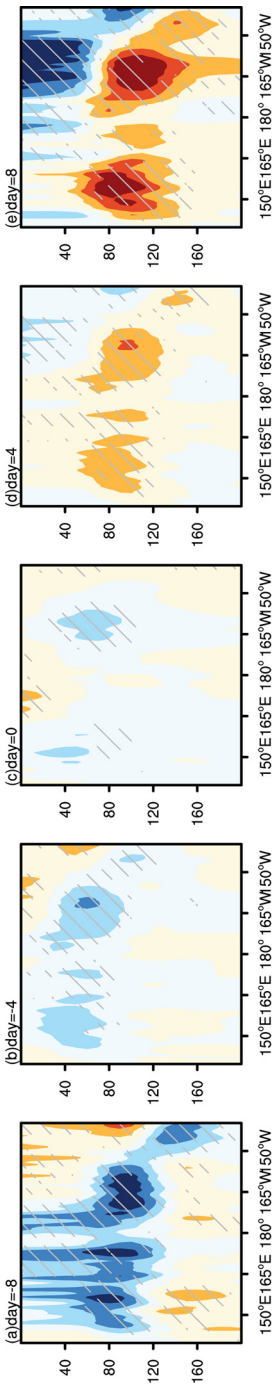

Fig. 9. PC2 lead-lag regression of oceanic temperature anomaly (shadings, unit: °C). The purple frame is the significant area at the subsurface layer. The areas marked by grey slashes passed the 0.05 significant level.

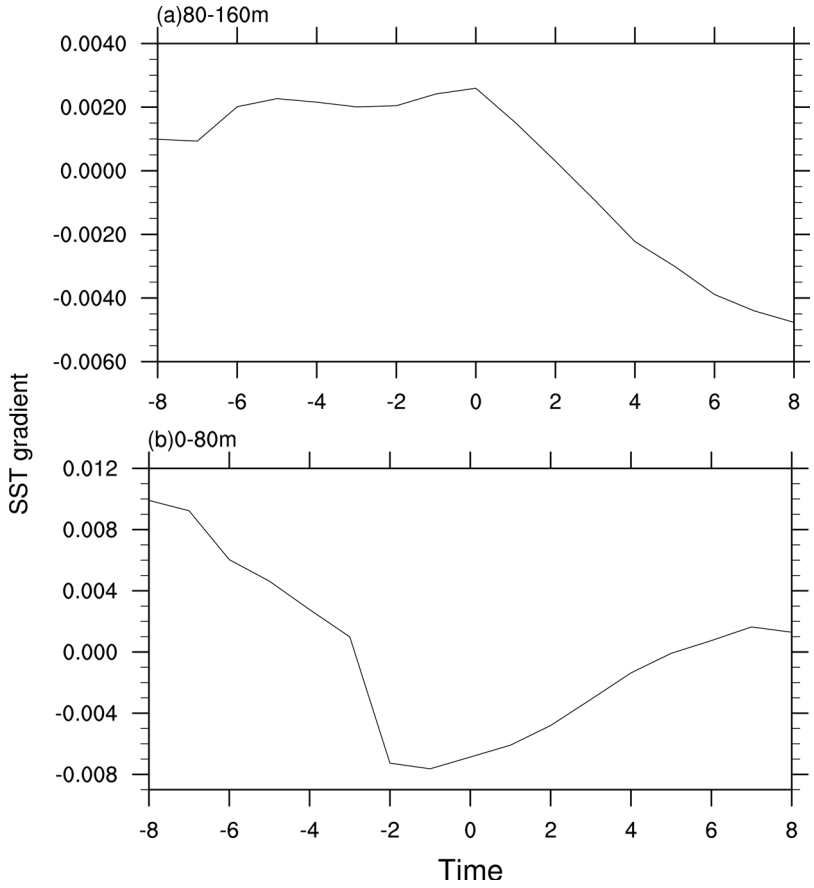

Fig. 10. Average sea surface temperature gradient anomaly in the subtropical front (24°-30 °N, 140 °E-140 °W) at different depths of EOF second modal events (unit: °C/100 km).

westerly wind. PC2 lag regression of physical quantities such as oceanic temperature is shown in Fig. 12. A weak cold oceanic temperature anomaly appears at the surface layer at day 0 to day 3. The air-sea temperature difference is small and the air-sea heat flux is not obvious. However, at this time, with the increasing of SST gradient, the westerly wind begins to increase, which increases the heat fluxes from the ocean to the atmosphere. Meanwhile, the sea surface is not only affected by the cold oceanic temperature at the subsurface layer. Due to the heat fluxes transporting from the ocean to the atmosphere, the cooling is intensified. It can be seen that a significant cold oceanic temperature anomaly appears at the surface layer at day 5 to day 8, which further increases the SST gradient. These make the westerly wind enhance and the heat fluxes increase. Accordingly, a positive air-sea feedback forms.

In general, the second mode of EOF analysis is a process in which the ocean affects the atmosphere. The cold oceanic temperature anomaly generates in the subsurface layer before day 0, and then passes up, which makes the SST gradient increasing. Then the westerly wind enhances because of the increasing baroclinic eddy growth rate, leading to more heat fluxes from ocean to the atmosphere, which results in a colder SSTA and a larger SST gradient. Consequently, a positive ocean-atmosphere feedback persists in the STFZ.

5. Summary and discussion

In this study, we focused on the relationship between the subsurface subtropical front and overlying atmosphere on subseasonal scale. Firstly, we investigated the position and intensity of the subsurface subtropical front. The subtropical oceanic front locates at the depth of 80–160 meters in the STFZ and the sea subsurface temperature gradient is significantly larger than that of surface subtropical oceanic front.

Then, two different physical processes between the surface and subsurface layer were found. We performed EOF analysis on oceanic temperature gradient in STFZ and got two different modes. The correlation coefficient between time series of the two modes is only $7.67*10^{-10}$, which confirms that they correspond to different air-sea coupled progresses. Therefore, we used time series of the two modes to perform lead-lag regressions on physical quantities from day -8 to day 8 and subtracted the average of these days to analyze the air-sea coupled processes the two modes correspond to. The results suggest that the first EOF mode shows a process in which the atmosphere affects the ocean. The increase of the westerly wind at day -8 causes a cold SSTA at day 0 by affecting the air-

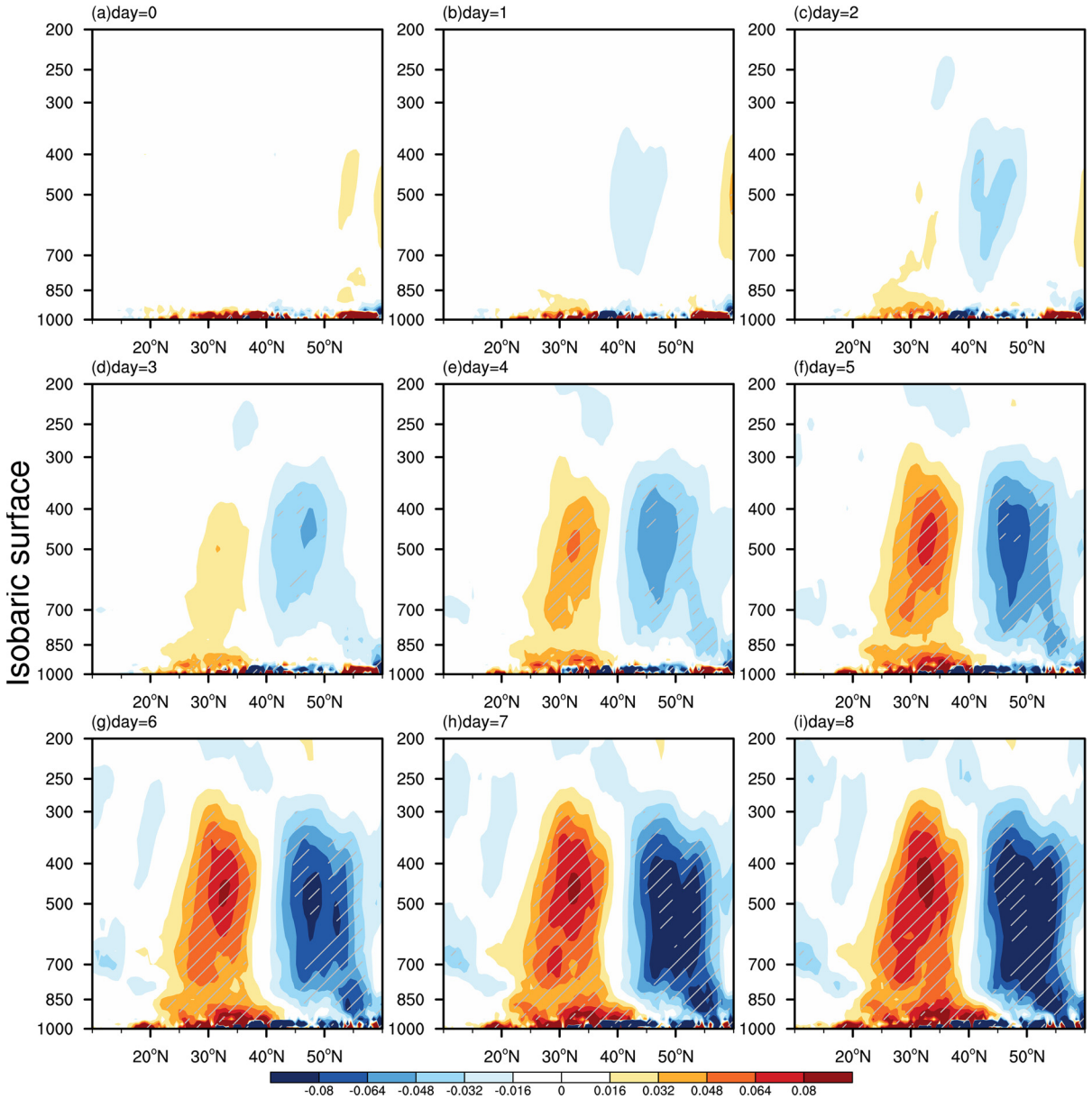

Fig. 11. PC2 lag regression of baroclinic eddy growth rate anomaly (shadings, unit: *10-5 m/s^3). The areas marked by grey slashes passed the 0.05 significant level.

sea heat flux, and it passes down after day 0, affecting the temperature of the subsurface ocean. The second EOF mode shows a process in which the ocean affects the atmosphere. The cold oceanic temperature anomaly generates in the subsurface layer at day -8 because of the increasing eastward flow and southward flow. Then it passes up, making the SST gradient increasing. At day 0, the baroclinic eddy growth rate shows a positive anomaly near the surface. Then the anomaly extended from lower troposphere to upper troposphere gradually. The enhanced atmospheric baroclinicity can accelerate the westerly wind. After that, the enhanced westerly wind leads to more heat fluxes from ocean to the atmosphere, which results in a colder SSTA and a larger SST gradient. A positive ocean-atmosphere feedback then persists.

In order to verify the above results obtained from regression analysis and analyze the variance of physical quantity these processes can explain, we composed the physical quantity of typical events from day -8 to day 8 and then subtracted the average of these days to highlight the variation. The results of the first mode are shown in Fig. 13. At day -8, the westerly wind enhances about 3 m/s and sensible and latent heat flux anomalies are about 2.4 W/m^2, 4.8 W/m^2 respectively. These lead to SST decreases and a cold SSTA about 0.04℃ appears at day 0. After that, the cold SSTA passes down, causing the sea subsurface temperature to decrease about 0.04℃ at day 8. Fig. 14 shows the results of the second mode. At day -8, cold oceanic temperature anomaly about 0.06℃ exists at the subsurface layer. Then, the anomaly passes up and cold SSTA appears. Due to the positive ocean-atmosphere feedback, the cold SSTA

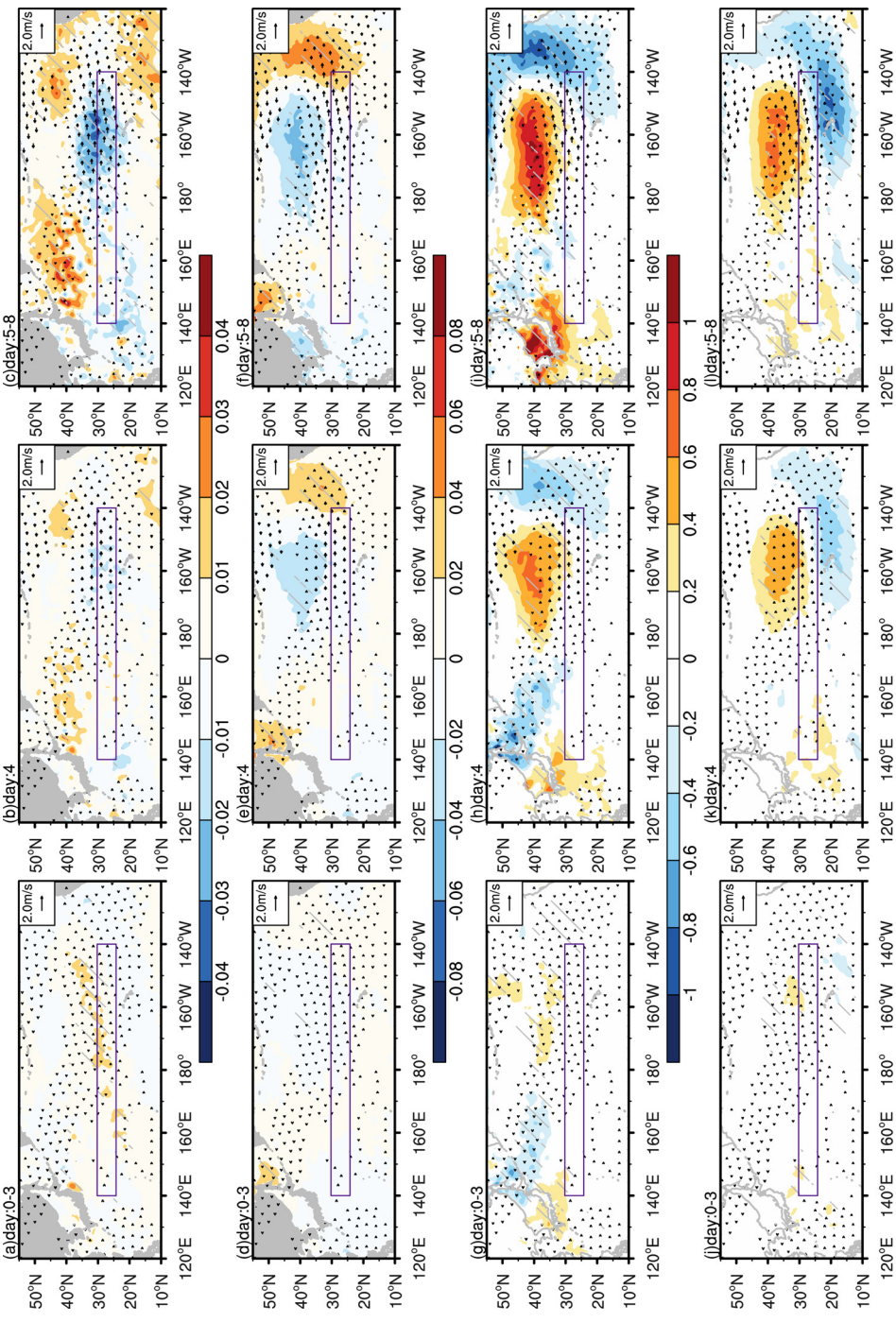

Fig. 12. PC2 lag regression of (a)-(c) sea surface temperature anomaly (shadings, unit: °C), (d)-(f) air-oceanic temperature difference anomaly (shadings, unit: °C), (g)-(i) sensible heat flux anomaly (shadings, unit: W/m^2), (j)-(l) latent heat flux anomaly (shadings, unit: W/m^2) and zonal wind anomaly at 200-300 hPa (arrows, unit: m/s). The purple frame is the location of the oceanic front. All arrows drawn passed 0.05 significant level. The areas marked by grey slashes passed the 0.05 significant level.

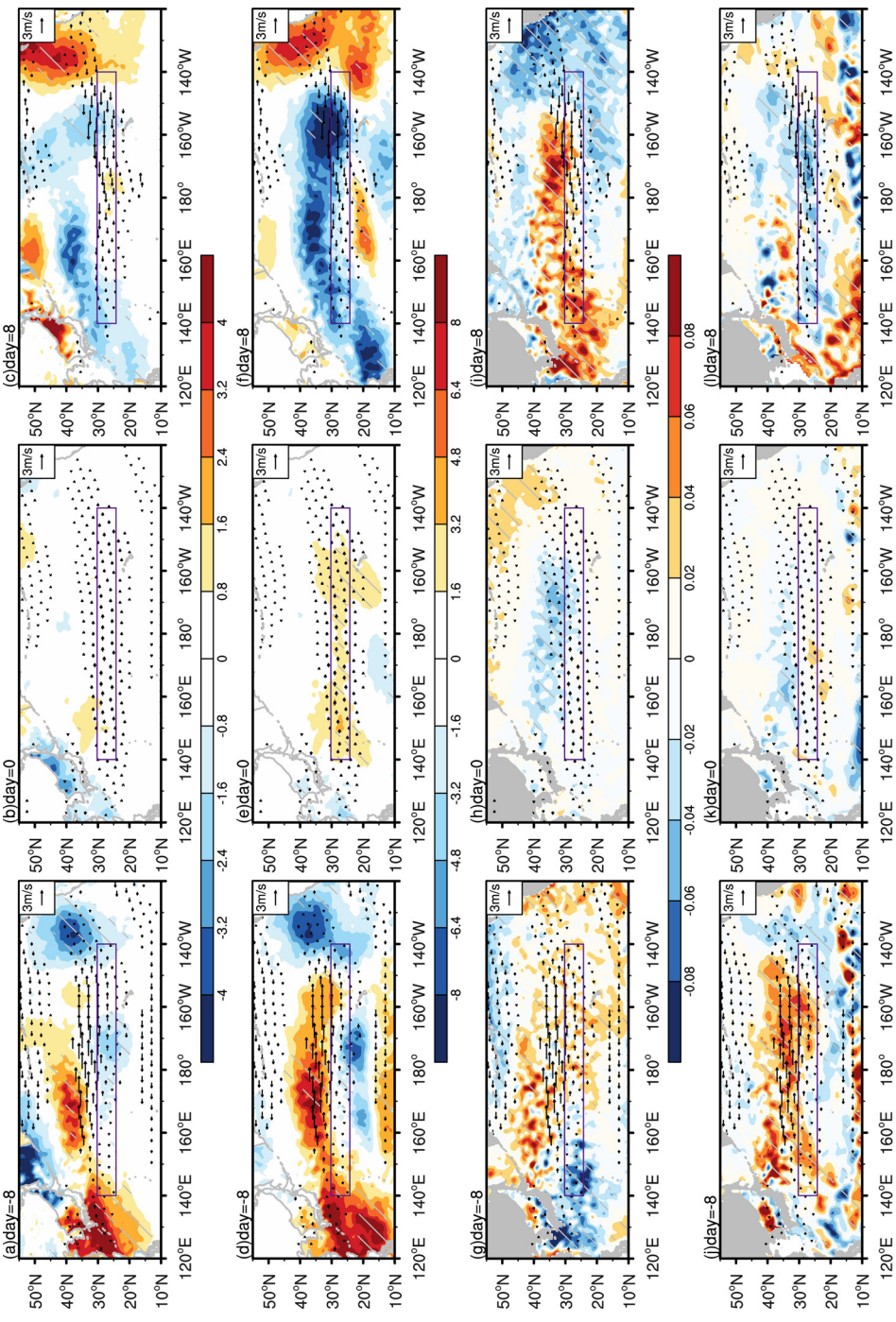

Fig. 13. Composite of (a)-(c) sensible heat flux anomaly (shadings, unit: W/m2), (d)-(f) latent heat flux anomaly (shadings, unit: W/m2), (g)-(i) sea surface temperature anomaly (shadings, unit: °C), (j)-(l) oceanic temperature anomaly at 80-160 m (shadings, unit: °C) and zonal wind anomaly at 200-300 hPa (arrows, unit: m/s) of the first modal events from days -8 to 8. The purple frame is the location of the oceanic front. All arrows drawn passed 0.05 significant level. The areas marked by grey slashes passed the 0.05 significant level.

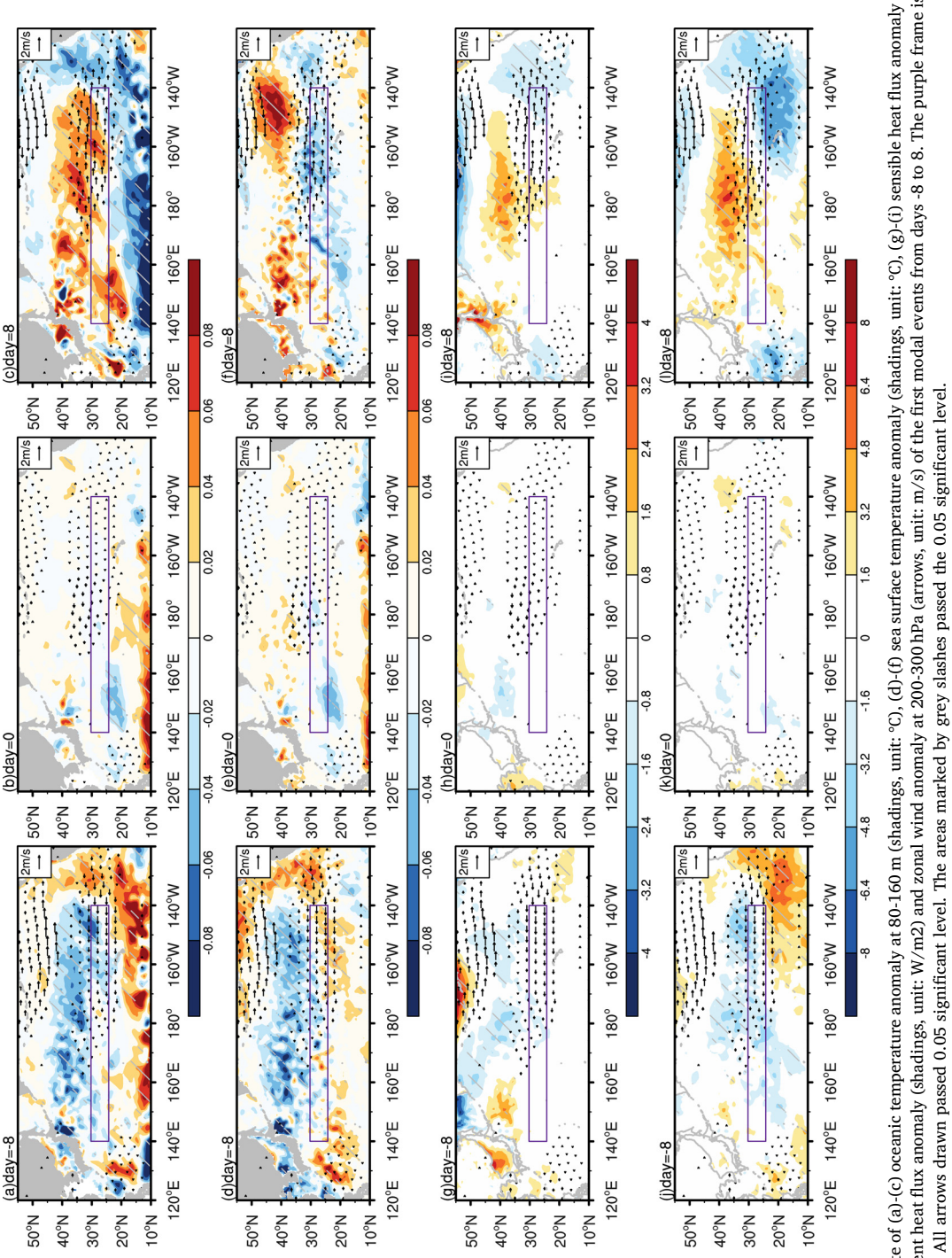

Fig. 14. Composite of (a)-(c) oceanic temperature anomaly at 80-160 m (shadings, unit: °C), (d)-(f) sea surface temperature anomaly (shadings, unit: °C), (g)-(i) sensible heat flux anomaly (shadings, unit: W/m2), (j)-(l) latent heat flux anomaly (shadings, unit: W/m2) and zonal wind anomaly at 200-300 hPa (arrows, unit: m/s) of the first modal events from days -8 to 8. The purple frame is the location of the oceanic front. All arrows drawn passed 0.05 significant level. The areas marked by grey slashes passed the 0.05 significant level.

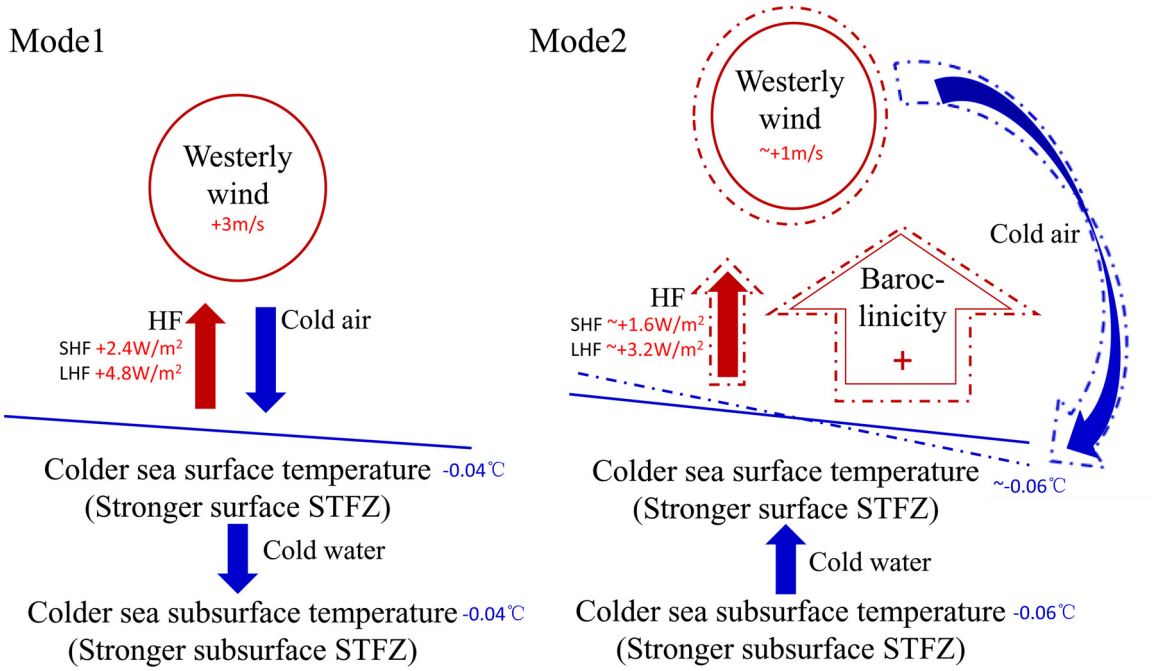

Fig. 15. The schematic diagram of two different air-sea coupled processes.

may be about 0.06℃ at day 8. At the same time, the westerly wind enhances about 1 m/s and sensible and latent heat flux anomalies are about 1.6 W/m^2, 3.2 W/m^2 respectively. The specific processes of the two modes are shown in Fig. 15.

It is worth noting that the SAFZ can also influence the atmospheric jet (Kobashi et al., 2008). In this study, we focus on the relationship between subsurface subtropical front and the atmospheric jet, the impact of the subarctic oceanic front is not considered. Besides, only CFSR dataset is used to investigate the air-sea coupled processes. Numerical simulation experiment will be carried out in future work.

CRediT authorship contribution statement

FeiFei Chen: Visualization, Investigation, Software, Data curation, Writing - original draft. **HaiBo Hu:** Conceptualization, Methodology, Writing - original draft, Supervision, Writing - review & editing. **Haokun Bai:** Visualization, Writing - review & editing.

Declaration of Competing Interest

The authors declare that they have no known competing financial interests or personal relationships that could have appeared to influence the work reported in this paper.

Acknowledgements

This work has benefited from discussions with William Perrie of BIO. This work was supported by the National Key Program for Developing Basic Science (grants 2016YFA0600303 and 2018YFC1505900), the National Natural Science Foundation of China (grants 41330420, 41621005, 41675064, 41675067, and 41875086). The authors are thankful for the support of the Jiangsu Provincial Innovation Center for Climate Change and Fundamental Research Funds for the Central University. This work was jointly supported by the Joint Open Project of KLME and CIC-FEMD (grant KLME201902). The NCEP/CFSR reanalysis data used in this study was obtained from https://rda.ucar.edu/datasets/ds093.0.

References

Alexander, M.A., Blade, I., Newman, M., Lanzante, J.R., Lau, N.C., Scott, J.D., 2002. The atmospheric bridge: the influence of ENSO teleconnections on air-sea interaction over the global oceans. J. Clim. 15, 2205–2231. https://doi.org/10.1175/1520-0442(2002)015<2205:TABTIO>2.0.CO;2.

Annis, J.L., White, W.B., 2003. Coupling of extratropical mesoscale eddies in the ocean to westerly winds in the atmospheric boundary layer. J. Phys. Oceanogr. 33 (5), 1095–1107. https://doi.org/10.1175/15200485(2003)033<1095:COEMEI>2.0.CO;2.

Aoki, Y., Suga, T., Hanawa, K., 2002. Subsurface subtropical fronts of the North Pacific as inherent boundaries in the ventilated thermocline. J. Phys. Oceanogr. 32 (8), 2299–2311. https://doi.org/10.1175/15200485(2002)032<2299:SSFOTN>2.0.CO;2.

Bai, H.K., Hu, H.B., Yang, X.Q., Ren, X.J., Xu, H.M., Liu, G.Q., 2019. Modeled MABL responses to the winter kuroshio SST front in the East China Sea and Yellow Sea. J.

Geophys. Res. Atmos. 124. https://doi.org/10.1029/2018JD029570.
Chen, Q., Hu, H., Ren, X., Yang, X.Q., 2019. Numerical simulation of midlatitude upper-level zonal wind response to the change of North Pacific subtropical front strength. J. Geophys. Res. Atmos. 124 (9), 4891–4912. https://doi.org/10.1029/2018JD029589.
Guan, W.N., Hu, H.B., Ren, X.J., Yang, X.Q., 2019. Subseasonal zonal variability of the western pacific subtropical high in summer: climate impacts and underlying mechanisms. Clim. Dyn. 5. https://doi.org/10.1007/s00382-019-04705-4.
Hashizume, H., Xie, S.P., Fujiwara, M., Shiotani, M., Watanabe, T., Tanimoto, Y., Liu, W.T., Takeuchi, K., 2002. Direct observations of atmospheric boundary layer response to SST variations associated with tropical instability waves over the eastern equatorial Pacific. J. Clim. 15 (23), 3379–3393. https://doi.org/10.1175/1520-0442(2002)015<3379:DOOABL>2.0.CO;2.
Hirata, H., Kawamura, R., Kato, M., Shinoda, T., 2016. Response of rapidly developing extratropical cyclones to sea surface temperature variations over the western Kuroshio-Oyashio confluence region. J. Geophys. Res. Atmos. 121 (8), 563–572. https://doi.org/10.1002/2015JD024391.
Kobashi, F., 2012. Review on North Pacific Subtropical Countercurrents and Subtropical Fronts: role of mode waters in ocean circulation and climate. J. Oceanogr. 68 (1), 21–43. https://doi.org/10.1007/s10872-011-0083-7.
Kobashi, F., Mitsudera, H., Xie, S.P., 2006. Three subtropical fronts in the North Pacific: observational evidence for mode water-induced subsurface frontogenesis. J. Geophys. Res. 111 (C9). https://doi.org/10.1029/2006JC003479. C09033.
Kobashi, F., Xie, S.P., Iwasaka, N., Sakamoto, T.T., 2008. Deep atmospheric response to the north pacific oceanic subtropical front in spring. J. Clim. 21 (22), 5960–5975. https://doi.org/10.1175/2008JCLI2311.1.
Kubokawa, A., Inui, T., 1999. Subtropical countercurrent in an idealized ocean GCM. J. Phys. Oceanogr. 29 (6), 1303–1313. https://doi.org/10.1175/1520-0485(1999)029<1303:SCIAIO>2.0.CO;2.
Liu, J.W., Zhang, S.P., Xie, S.P., 2013. Two types of surface wind response to the East China Sea Kuroshio front. J. Clim. 26 (21), 8616–8627. https://doi.org/10.1175/JCLI-D-12-00092.1.
Liu, G.Q., Perrie, W., Kudryavtsev, V., He, Y., Shen, H., Zhang, B., Hu, H.B., 2016. Radar imaging of intense nonlinear Ekman divergence. Geophys. Res. Lett. 43 (18), 9810–9818. https://doi.org/10.1002/2016GL070799.
Minobe, S., Kuwanoyoshida, A., Komori, N., Xie, S.P., Small, R.J., 2008. Influence of the gulf stream on the troposphere. Nature. 452 (7184), 206–209. https://doi.org/10.1038/nature06690.
Nakamura, H., Sampe, T., Goto, A., Ohfuchi, W., Xie, S.P., 2008. On the importance of midlatitude oceanic frontal zones for the mean state and dominant variability in the tropospheric circulation. Geophys. Res. Lett. 35, L15709. https://doi.org/10.1029/2008GL034010.
Namias, J., Cayan, D.R., 1981. Large-scale air-sea interactions and short-period climatic fluctuations. Science. 214, 869–876. https://doi.org/10.1126/science.214.4523.869.
North, G.R., Bell, T.L., Cahalan, R.F., Moeng, F.J., 1982. Sampling errors in the estimation of empirical orthogonal functions. Mon. Wea. Rev. 110 (7), 699–706. https://doi.org/10.1175/15200493(1982)110<0699:SEITEO>2.0.CO;2.
O'Neill, L.W., Chelton, D.B., Esbensen, S.K., 2003. Observations of SST-induced perturbations of the wind stress field over the Southern Ocean on seasonal timescales. J. Clim. 16 (14), 2340–2353. https://doi.org/10.1175/2780.1.
Parfitt, R., Czaja, A., Minobe, S., Kuwano-Yoshida, A., 2016. The atmospheric frontal response to SST perturbations in the Gulf Stream region. Geophys. Res. Lett. 43 (5), 2299–2306. https://doi.org/10.1002/2016GL067723.
Qiu, C., Kawamura, H., Mao, H., Wu, J., 2015. Mechanisms of the disappearance of sea surface temperature fronts in the subtropical North Pacific Ocean. J. Geophys. Res. Oceans 119, 4389–4398. https://doi.org/10.1002/2014JC010142.
Saha, S., et al., 2010. The NCEP climate forecast system reanalysis. Bull. Am. Meteorol. Soc. 91 (8), 1015–1057. https://doi.org/10.1175/2010BAMS3001.1.
Shimada, T., Kawamura, K., 2008. Satellite evidence of wintertime atmospheric boundary layer responses to multiple SST fronts in the Japan Sea. Geophys. Res. Lett. 35 (35), 186–203. https://doi.org/10.1029/2008GL035810.
Small, R.J., Deszoeke, S.P., Xie, S.P., O'Neill, L., Seo, H., Song, Q., Cornillon, P., Spall, M., Minobe, S., 2008. Air–sea interaction over ocean fronts and eddies. Dyn. Atmos. Oceans. 45, 274–319. https://doi.org/10.1016/j.dynatmoce.2008.01.001.
Small, R.J., Tomas, R.A., Bryan, F.O., 2014. Storm track response to ocean fronts in a global high-resolution climate model. Clim. Dyn. 43 (3–4), 805–828. https://doi.org/10.1007/s00382-013-1980-9.
Suga, T., Hanawa, K., 1990. The mixed-layer climatology in the northwestern part of the North Pacific subtropical gyre and the formation area of Subtropical Mode Water. J. Mar. Res. 48 (3), 543–566. https://doi.org/10.1357/002224090784984669.
Tokinaga, H., Tanimoto, Y., Nonaka, M., Taguchi, B., Fukamachi, T., Xie, S.P., Nakamura, H., 2006. Atmospheric sounding over the winter Kuroshio Extension: effect of surface stability on atmospheric boundary layer structure. Geophys. Res. Lett. 33 (4), 355–363. https://doi.org/10.1029/2005GL025102.
Vecchi, G.A., Xie, S.P., Fischer, A.S., 2004. Ocean-atmosphere covariability in the Western Arabian Sea. J. Clim. 17 (6), 1213–1223. https://doi.org/10.1175/1520-0442(2004)017<1213:OCITWA>2.0.CO;2.
Wallace, J.M., Smith, C.A., Jiang, Q., 1990. Spatial patterns of atmosphere–ocean interaction in the northern winter. J. Clim. 3 (9), 990–998. https://doi.org/10.1175/1520-0442(1990)003<0990:SPOAOI>2.0.CO;2.
Wang, L.Y., Hu, H.B., Yang, X.Q., Ren, X.J., 2016. Atmospheric eddy anomalies associated with the wintertime North Pacific subtropical front strength and their influences on the seasonal-mean atmosphere. Sci China Earth Sci. 59, 1–15. https://doi.org/10.1007/s11430-016-5331-7.
Wang, L.Y., Hu, H.B., Yang, X.Q., 2018. The atmospheric responses to the intensity variability of subtropical front in the wintertime North Pacific. Clim. Dyn. 2018, 1–17. https://doi.org/10.1007/s00382-018-4468-9.
Xie, S.P., 2004. Satellite observations of cool ocean–atmosphere interaction. Bull. Amer. Meteor. Soc. 85 (2), 195–208.
Xu, M., Xu, H., 2015. Atmospheric responses to Kuroshio SST front in the East China Sea under different prevailing winds in winter and spring. J. Clim. 28 (8), 3191–3211. https://doi.org/10.1175/JCLI-D-13-00675.1.
Xu, H., Xu, M., Xie, S.P., Wang, Y., 2011. Deep atmospheric response to the spring Kuroshio over the East China Sea. J. Clim. 24 (18), 4959–4977.
Xu, L., Xie, S.P., Liu, Q., 2012. Mode water ventilation and subtropical countercurrent over the North Pacific in CMIP5 simulations and future projections. J. Geophys. Res. Oceans 117 (C12). https://doi.org/10.1029/2012JC008377.
Yao, Y., Zhong, Z., Yang, X.Q., 2016. Numerical experiments of the storm track sensitivity to oceanic frontal strength within the Kuroshio/Oyashio Extensions. J. Geophys. Res. Atmos. 121 (6), 2888–2900. https://doi.org/10.1002/2015JD024381.
Zhang, L.Y., Xu, H.M., Shi, N., Deng, J.C., 2017. Responses of the East Asian jet stream to the North Pacific subtropical front in spring. Adv Atmos Sci. 34, 144–156. https://doi.org/10.1007/s00376-016-6026-x.